

Journal of Mechanics of Materials and Structures

**DYNAMIC FRACTURE TESTS OF POLYMETHYLMETHACRYLATE
USING A SEMICIRCULAR BEND TECHNIQUE**

Sheng Huang, Sheng-Nian Luo, Bryan S. A. Tatone and Kaiwen Xia

Volume 6, No. 6

July–August 2011

DYNAMIC FRACTURE TESTS OF POLYMETHYLMETHACRYLATE USING A SEMICIRCULAR BEND TECHNIQUE

SHENG HUANG, SHENG-NIAN LUO, BRYAN S. A. TATONE AND KAIWEN XIA

We adopt a recently developed technique, dynamic semicircular bend testing, to measure the fracture initiation toughness, fracture propagation toughness, and fracture velocity of polymethylmethacrylate (PMMA). A modified split Hopkinson pressure bar system is used to apply the dynamic load. In this method, both the fracture initiation toughness and fracture energy, and thus the average fracture propagation toughness, are determined. The initiation toughness is found to be similar to the propagation toughness, and both toughnesses are loading rate-dependent. Our initiation toughness values for PMMA are in accord with those reported in the independent literature. The fracture velocity increases and then becomes saturated as the propagation toughness increases. We also measure the fracture surface roughness of the recovered fragments. While the surface roughness increases with the fracture energy, the increase of surface area alone is not sufficient to accommodate the increase in fracture energy, suggesting other energy dissipation mechanisms in the dynamic fracture process besides free surface creation.

1. Introduction

Polymethylmethacrylate (PMMA) is a homogeneous and isotropic polymer that is widely used in many applications for its transparency, high yield strength, and low density and cost. However, it is brittle at room temperature. There is a sustained interest in understanding fracture in such polymers. Many studies have been conducted on the fracture of PMMA under quasistatic conditions [Kobayashi et al. 1972], while limited attempts have been made to measure the dynamic fracture properties of brittle solids (including PMMA), primarily due to the difficulties in experimentation and subsequent data interpretation [Maigre and Rittel 1995]. For example, a significant inertial effect can exist during high-loading rate loading as demonstrated by Böhme and Kalthoff [1982]. In their experiments, a three-point bend sample was loaded dynamically by a drop weight, and they showed that the crack tip stress intensity factor (SIF) history measured with the shadow optical method of caustics did not synchronize with the load histories at the supporting points due to the inertial effect. This inertial effect may subsequently complicate the data reduction and interpretation.

The inertial effect on the fracture toughness can be separated with optical methods [Dally 1979; Kobayashi and Dally 1977b; Rosakis et al. 1984; Xia et al. 2006], which normally require high-speed photography. For other testing methods, the inertial problem can be circumvented with the combination of experimental measurements and numerical simulations [Maigre and Rittel 1995], but this process is rather tedious to apply. Recently, Owen et al. [1998] observed that the SIFs obtained by directly

This work has been supported by NSERC/Discovery Grant No. 72031326. LANL is under the auspices of the U.S. Department of Energy under contract No. DE-AC52-06NA25396.

Keywords: dynamic fracture, PMMA, fracture toughness, semicircular bend, fracture velocity, surface roughness.

measuring the crack tip opening are consistent with those calculated with the quasistatic equation when the dynamic stress equilibrium of the specimen is roughly achieved in split Hopkinson tension bar testing. This concept was subsequently adopted in [Weerasooriya et al. 2006] for ceramics in split Hopkinson pressure bar (SHPB) testing using a dynamic four-point bend method.

For static fracture, there is only one fracture toughness, namely fracture initiation toughness. Fracture initiation toughness is also relevant in dynamic fracture. There are a few studies on dynamic initiation toughness for PMMA [Wada 1992; Wada et al. 1993; Rittel and Maigre 1996]. In addition, there is a fracture propagation toughness that characterizes material resistance to a propagating crack during dynamic fractures. Because propagation toughness is directly related to energy consumption during fracture failure processes, it is desirable to measure both toughnesses for dynamic fractures. Fracture propagation toughness is usually measured using optical methods for transparent polymers or polished metals [Kobayashi and Dally 1977b; Dally 1979; Rosakis et al. 1984; Xia et al. 2006]. In a recently developed dynamic semicircular bend (SCB) method [Chen et al. 2009], fracture initiation toughness, fracture energy (and thus average fracture propagation toughness), and average fracture velocity can be measured simultaneously. The measurement of fracture energy also allows us to gain insight into the energy dissipation mechanisms during dynamic fractures.

The fracture propagation toughness is commonly a monotonically increasing function of crack velocity. This relationship was first proposed in [Kobayashi and Dally 1977a; Dally 1979] for PMMA using a dynamic photoelasticity method. Rosakis et al. [1984] reached a similar conclusion using wedge loaded cantilever beam specimens made of AISI 4030 steel. More evidence for this dependence was subsequently observed by using three-point bend specimens loaded in a drop weight tower in [Zehnder and Rosakis 1990]. At low fracture speed, the dependence of SIF on fracture velocity is weak, while at higher crack speeds it becomes quite pronounced. As the fracture velocity is close to its limiting value, the fracture toughness can be very large as compared to the static value. This leads to the notion of a limiting fracture velocity beyond which the fracture cannot propagate no matter how hard it is driven. Similar results were also observed for 2024-T3 aluminum [Owen et al. 1998]. Other researchers, for instance Évora et al. [2005], clearly observed that the SIF continues to increase under a constant maximum velocity, supporting the limiting fracture velocity postulation. This limiting fracture velocity during dynamic loading is also of interest for PMMA.

In this study, we use the semicircular bend (SCB) method (originally proposed in [Chong and Kuruppu 1984] and extended in [Chen et al. 2009] to dynamic testing for brittle materials) to perform fracture testing on PMMA with split Hopkinson pressure bar (SHPB) and notched SCB specimens. Section 2 addresses the SCB sample preparation and SHPB setup for SCB testing, and Section 3, the measurement techniques and data reduction methodology. The results and discussion on the initiation and propagation fracture toughnesses, and fracture velocity under different loading rates, are presented in Section 4. This section also discusses the correlation between fracture surface toughness and fracture energy as regards the energy dissipation mechanisms during dynamic fracture. Conclusions are given in Section 5.

2. Experimental setup and sample preparation

A 25 mm diameter SHPB system (Figure 1) is used to apply the dynamic load. The bars are made of 7075 aluminum alloy, which has a yielding strength of 455 MPa and Young's modulus of 71.8 GPa. The

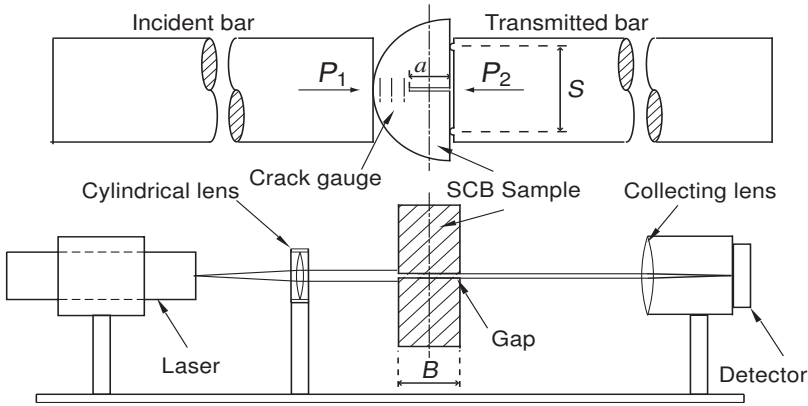


Figure 1. Schematics of the SHPB system, notched SCB sample, and LGG system.

lengths of the striker, incident, and transmitted bars are 300 mm, 2500 mm, and 1500 mm, respectively. The strain gauge stations on the incident and transmitted bars are 933 mm and 500 mm away from the respective bar-sample interfaces. When the striker bar impacts the incident bar, a compressive wave is generated and propagates into the sample (see Figure 1). The interaction of the incident wave with the sample results in two waves: the reflected wave propagating back into the incident bar and the transmitted wave propagating into the transmitted bar. The incident wave, reflected wave, and transmitted wave are denoted with subscripts i , r , and t , respectively. The respective loading forces on the incident and transmitted ends of the specimen are:

$$P_1 = AE(\varepsilon_i + \varepsilon_r), \quad P_2 = AE\varepsilon_t, \quad (1)$$

where E is the Young's modulus of the bar material, A is the cross-sectional area of the bar, and ε are the strains. The strain gauge signals are relayed to the Wheatstone bridge circuits, amplified, and then recorded by an eight-channel Sigma digital oscilloscope (Nicolet). The striker velocity is measured by a laser-detector system.

A PMMA rod (radius $R = 19.05$ mm) is sliced into discs (thickness $B = 16$ mm) that are in turn split into semicircular shapes. A 1.6 mm wide and 6 mm long notch is then introduced into the sample, with a sharp tip of radius 0.15 mm (Figure 2). This radius is comparable to that used in the dynamic fracture tests of PMMA of [Maigre and Rittel 1995]. For compression-bend loading, the SCB specimen is placed in tangential contact with the incident bar and in point contact with two pins on the transmitted bar separated by a distance S (see Figure 1).

We adopt a laser gap gauge (LGG) system to measure the time-resolved crack surface opening displacement (CSOD; see Figure 1). The details of the LGG system are presented in [Chen et al. 2009]. The amount of light passing through the notch increases with increasing notch width during opening, and is recorded by the LGG system as voltage signals. The voltage is linearly proportional to the gap width and thus the CSOD. Because PMMA is transparent, blue ink is sprayed on the specimen near the notch region to block the laser light except in the notched area (Figure 2a). To measure the crack propagation velocity, three 0.5 mm (in diameter) pencil leads and break-wire circuits are attached to the sample with instant brittle glue as crack gauges. They essentially detect the onset of fracture at three different positions. The

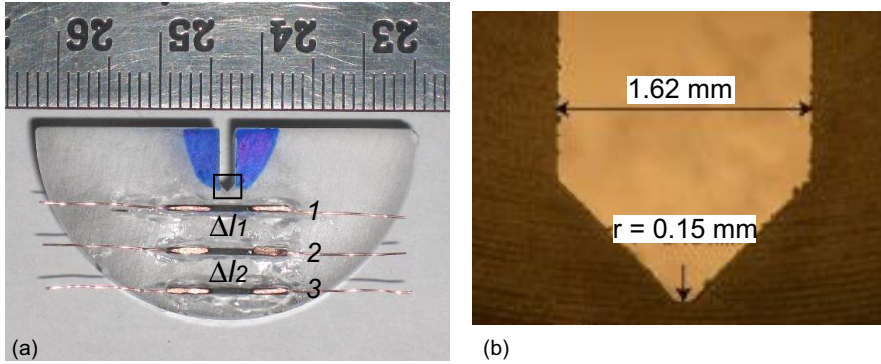


Figure 2. (a) Photo of a PMMA SCB sample with crack gauges 1–3. A fine division in the scale denotes 1 mm. (b) Amplified image of the region marked with a rectangle in (a), showing the crack and tip dimensions.

leads are flattened along the axis in order to improve their bonding strength with the PMMA specimen.

It is critical to achieve dynamic force balance in the specimen during dynamic loading. To this end, we utilize the pulse shaper technique, which was detailed in [Frew et al. 2005]. In traditional SHPB tests, the sharp rising front of the incident wave causes a sudden increase of load in the sample at the end in contact with the incident bar. For brittle materials, this type of load may induce undesired damage to the sample, leading to significant complications and possibly errors in interpreting the measurements. We used a black rubber disc of 2.5 mm diameter and 2 mm thickness as the pulse shaper. This method normally yields an incident pulse with a ramp front of about $100 \mu\text{s}$ in duration, which allows the sample to achieve force balance throughout the loading stage of the deformation.

Figure 3 shows the forces on both ends of the specimen in a typical test. Equation (1) states that the dynamic force on the incident-bar side of the specimen (P_1) is proportional to the sum of the incident (In) and reflected (Re) stress waves, and that on the transmission-bar side (P_2) to the transmitted (Tr) stress wave. For SCB tests, P_2 is equally distributed to the two supporting pins. As shown in Figure 3,

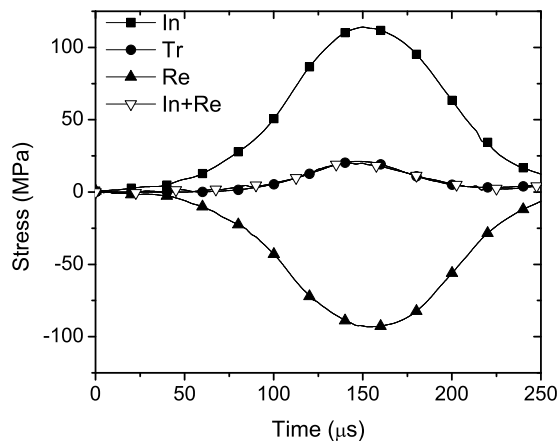


Figure 3. Dynamic force histories in a typical dynamic SCB test.

the dynamic forces on both sides of the specimen are almost identical during the entire dynamic loading period. Inertial effects are thus approximately eliminated because there is no global force difference in the specimen. Given negligible inertial effects, we can then perform quasistatic analysis [Chen et al. 2009].

3. Measurement techniques and data reduction

3.1. Loading history and fracture velocity. Figure 4 shows the loading history (P_2) and corresponding CSOD history during a dynamic SCB test. We denote the time zero (A) as the arrival time of the incident pulse at the sample. Because dynamic force balance is achieved, time instant B ($102 \mu\text{s}$), when the load reaches its peak, corresponds to the fracture initiation in the specimen, as in a quasistatic experiment. The slope of the CSOD increases with time and approaches a terminal constant beginning at instant C ($136 \mu\text{s}$). The two vertical lines passing through points B and C divide the entire deformation period into three stages. In stage I, the crack opens up elastically; in stage II, the crack propagates dynamically; in stage III, the fracture separates the sample completely into two pieces. The terminal separation velocity of the two fragments is the linear slope in CSOD after instant C . This velocity $v = 12.3 \text{ m/s}$ is twice the individual fragment terminal velocity. At instant D ($180 \mu\text{s}$), the completely separated fragments fly further away from each other.

We use high-speed photographs to illustrate qualitatively these representative instants (Figure 5). These photos are taken with a Photron SA-1 high-speed camera at 180 thousand frames per second. Each frame contains 125×125 pixels. Figure 5 shows the crack initiation at instant B , complete fracture at instant C , and pure rotation of the fragments with respect to the contact point of the specimen with the incident bar at instant D , consistent with the strain gauge measurements (Figure 4). The gauges were glued on the other side of the specimen for this test.

Crack propagation lasts about $\Delta t_{BC} = 34 \mu\text{s}$. Given the crack distance $L_s = R - a = 12.7 \text{ mm}$ for this test, we estimate the average crack growth velocity as $v_f = 374 \text{ m/s}$. We also use crack gauges to estimate

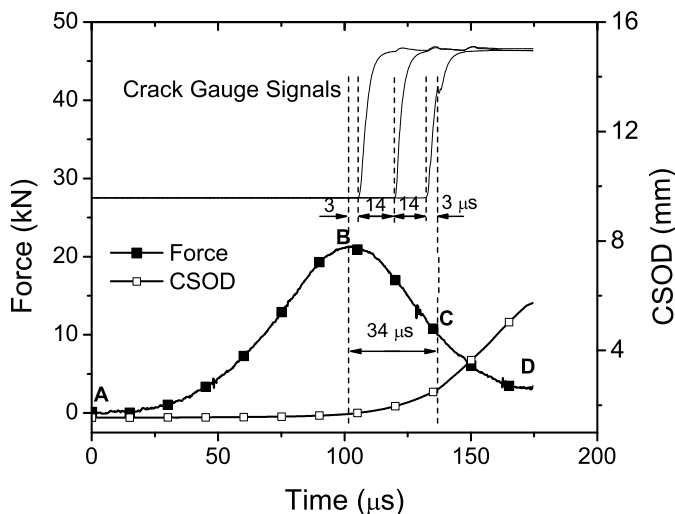


Figure 4. Typical loading history and CSOD history of the SCB specimen tested in SHPB. Top inset: crack gauge signals at three locations.

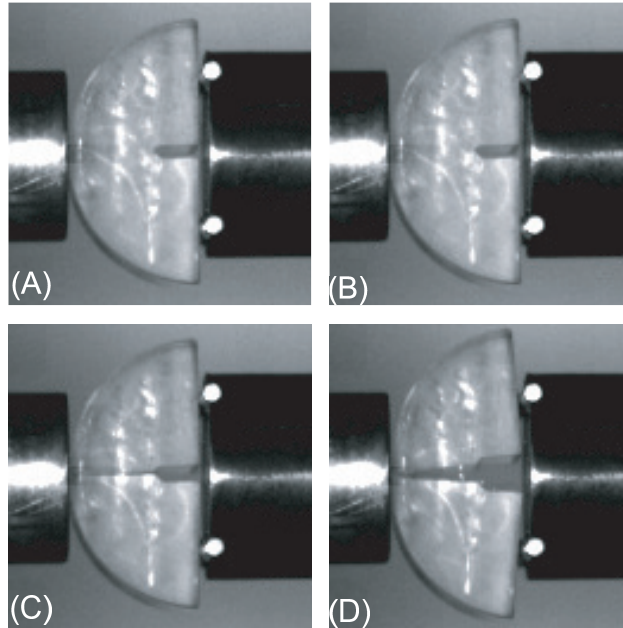


Figure 5. High-speed camera snapshots of a dynamic SCB test. A: time zero, B: $\sim 102 \mu\text{s}$, C: $\sim 136 \mu\text{s}$, D: $\sim 180 \mu\text{s}$.

the fracture propagation velocity. Three crack gauges made of pencil lead are separated by $\Delta l_1 = 5.55 \text{ mm}$ and $\Delta l_2 = 4.43 \text{ mm}$ (see Figure 2). The time separations between the arrivals of the fracture onset signals are $\Delta t_1 = 14 \mu\text{s}$, and $\Delta t_2 = 14 \mu\text{s}$, respectively (see Figure 4). Thus the corresponding average fracture velocities are $v_1 = 396 \text{ m/s}$, and $v_2 = 309 \text{ m/s}$. The fracture velocity appears to decrease as the crack propagates during dynamic loading. The first gauge is cemented at about 1.2 mm away from the crack tip in order to avoid interfering with crack initiation. This explains the $3 \mu\text{s}$ delay between the crack initiation and the breaking of the first crack gauge. The fracture velocity as measured with LGG is consistent with the crack gauge results. One advantage of the LGG is that it is a noncontact method.

3.2. Calculation of initiation fracture toughness. The stress intensity factor (SIF) of the mode-I fracture of the SCB specimen can be calculated from (2), in analogy to the rectangular three-point bending method in the ASTM standard E399-06e2 [ASTM 1997]:

$$K_I(t) = \frac{P(t)S}{BR^{3/2}}Y(a/R), \quad (2)$$

where $P(t)$ is the measured load force history, and $Y(a/R)$ a dimensionless geometry factor which can be calculated with a standard finite element software package (for example, ANSYS) [Barsoum 1977]. The initiation fracture toughness K_{IC}^d corresponds to the peak load P_{\max} [Chen et al. 2009].

3.3. Calculation of propagation fracture energy and toughness. The propagation fracture energy and fracture toughness can be deduced based on energy conservation and the strain gauge and LGG measurements. Similarly, Zhang et al. [2000] used a high-speed camera instead of a LGG to estimate the fragment residual velocities. The energy carried by a stress wave (incident, reflected, or transmitted) is

[Kolsky 1953]:

$$W = \int_0^t E \varepsilon^2 A C d\tau, \quad (3)$$

where E is the Young's modulus, A is the cross-sectional area, and C is the wave speed of the bar. The total energy absorbed by the specimen then is $\Delta W = W_i - W_r - W_t$. Part of the total energy absorbed is used to create new crack surfaces, namely the total fracture energy W_G ; the other part remains in the fragments as the residue kinetic energy (K). That is, $\Delta W = W_G + K$. Note that there may be some residual strain energy in the fragments. However, the fragment releases the strain energy at the speed of elastic wave velocity; the strain energy release is virtually at the same pace as the release of the far-field load. We thus assume that this strain energy is negligible.

For the rotating fragments, the moment of inertia is I , and the total rotational kinetic energy is $K = I\omega^2/2$, where the fragment angular velocity ω is estimated from the CSOD data. The average propagation fracture energy is $G_c = W_G/A_c$, where A_c is the area of the crack surfaces created. Here we use the projected area for the crack surface area. Assuming the plane strain, the average dynamic propagation fracture toughness is:

$$K_I^P = \sqrt{G_c E / (1 - \nu^2)}, \quad (4)$$

where $E = 3.24$ GPa and $\nu = 0.35$ are the Young's modulus and Poisson's ratio of the specimen respectively, with the values taken from the literature [Needleman and Rosakis 1999].

4. Results and discussion

Fifteen SCB samples of PMMA are tested at various impact velocities, and all of them are split cleanly into two equal pieces with smooth fracture surfaces, as shown in Figure 6. The results are summarized in Table 1, including loading rate \dot{K}_I , initiation fracture toughness K_{IC}^d , total fracture energy W_G , average fracture energy G_C , average crack growth velocity v_f , and propagation fracture toughness K_I^P .

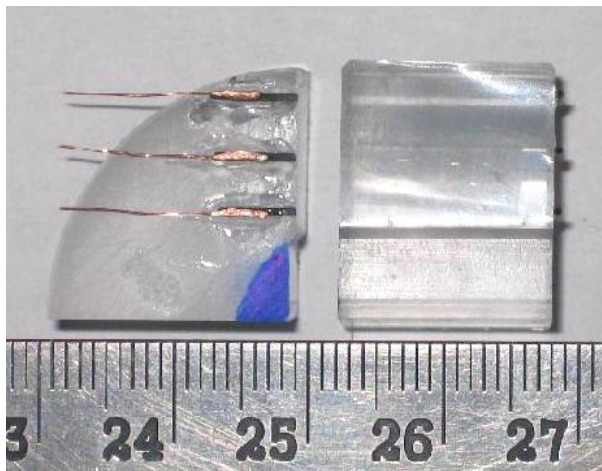


Figure 6. Typical PMMA samples recovered after fracture: side view (left) and fracture surface (right).

Sample	\dot{K}_I (GPa m ^{1/2} /s)	v_f (m/s)	K_{IC}^d (MPa m ^{1/2})	W_G (J)	G_c (J/m ²)	K_I^P (MPa m ^{1/2})
1	19	267	2.46	0.24	5.97×10^2	1.50
2	22	285	2.61	0.35	8.56×10^2	1.80
3	30	270	2.63	0.23	5.83×10^2	1.48
4	49	283	2.70	0.35	8.55×10^2	1.79
5	54	328	2.77	0.45	1.11×10^3	2.04
6	71	338	3.68	0.93	2.26×10^3	2.91
7	74	342	3.61	0.99	2.47×10^3	3.05
8	79	356	3.28	0.52	1.29×10^3	2.20
9	86	357	3.79	0.80	1.97×10^3	2.72
10	117	365	4.91	2.10	5.52×10^3	4.69
11	121	358	5.17	2.20	5.68×10^3	4.56
12	142	377	9.60	3.51	8.61×10^3	5.69
13	145	374	7.57	6.95	1.72×10^4	8.06
14	160	375	8.08	6.53	1.62×10^4	7.82
15	169	369	8.69	7.54	1.89×10^4	8.44

Table 1. Summary of experimental results.

4.1. Loading rate effect. The loading rate may have a considerable effect on the fracture toughness of a solid under dynamic loading. We characterize the loading rate with \dot{K}_I obtained from the time evolution of SIF (K_I). Figure 7 shows loading and unloading in terms of SIF in a typical test. During the loading period, K_I increases with time and then reaches a constant (maximum) during 75–100 μ s, followed by a drop before unloading; this maximum loading rate is adopted as the loading rate in a specific test, and also denoted as \dot{K}_I for simplicity. In this work, fifteen different loading rates are explored; for each loading rate, the initiation and propagation fracture toughnesses of a SCB specimen are determined (see Table 1 and Figure 8).

Both the initiation and propagation fracture toughnesses increase with loading rate. At a given loading rate, the initiation fracture toughness is slightly higher than the propagation toughness (except in one case

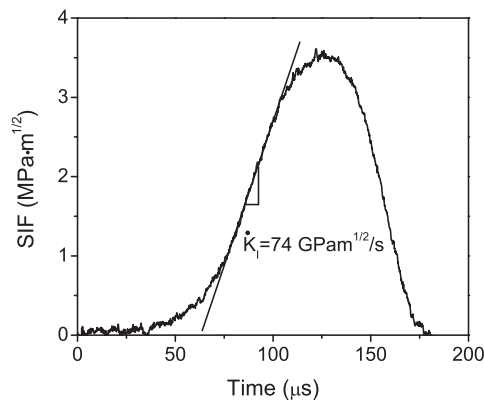


Figure 7. Typical SIF-time curve for determining loading rate.

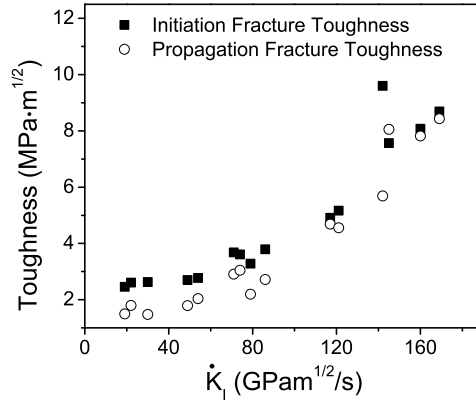


Figure 8. Initiation and propagation toughnesses of PMMA under different loading rates.

at 145 GPam^{1/2}/s). From the roughness measurement discussed below, the fracture surfaces are smooth. However, there is a finite radius at the tip of the notch prefabricated for crack initiation, which may lead to larger initiation toughness.

Figure 9 compares our results for fracture toughness with those reported in the literature [Wada 1992; Wada et al. 1993; Rittel and Maigre 1996]. It can be seen that at high loading rates (10⁴–10⁵ MPa m^{1/2}/s), our data agree well with those of this last reference, further confirming the validity of the dynamic SCB method. The dynamic SCB method has advantages such as simplicity. Our result at low loading rates is also in accord with previous data.

The fracture toughness (\dot{K}_I) data can be described with an exponential form:

$$K_I^d / K_{I0} = \exp(\dot{K}_I / \dot{K}_{I0}), \tag{5}$$

where K_{I0} and \dot{K}_{I0} are fitting parameters. Fitting (3) to our data only yields $K_{I0} = 1.85 \text{ MPa m}^{1/2}$ and $\dot{K}_{I0} = 1.0 \times 10^5 \text{ MPa m}^{1/2}/\text{s}$ in the loading rate range of 10⁻¹–10⁵ MPa m^{1/2}/s (dashed curve, Figure 9). If both present and previous data are used, we obtain $K_{I0} = 1.47 \text{ MPa m}^{1/2}$ and $\dot{K}_{I0} = 1.2 \times 10^5 \text{ MPa m}^{1/2}/\text{s}$ (solid line, Figure 9) in a wide range of loading rates (10⁻²–10⁵ MPa m^{1/2}/s).

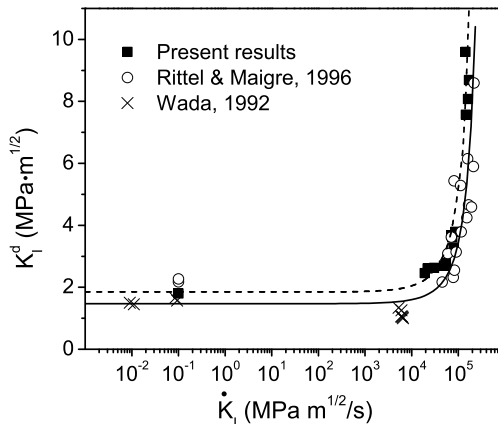


Figure 9. Comparison of previous and present initiation fracture toughness results.

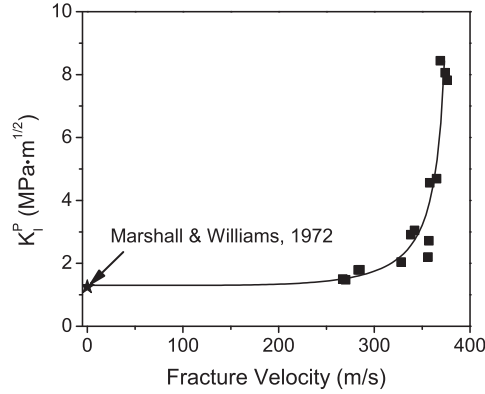


Figure 10. The fracture velocity-propagation toughness curve.

Further experiments are desirable to establish whether these results can be extrapolated to even lower or higher loading rates.

4.2. Fracture velocity. The propagation fracture toughness is believed to be a function of fracture velocity [Zehnder and Rosakis 1990]. Our experiments show the increase of propagation fracture toughness K_I^P with increasing fracture velocity (Figure 10). For example, K_I^P is $7.82 \text{ MPa m}^{1/2}$ at the highest fracture velocity (386 m/s) achieved, and decreases to $1.5 \text{ MPa m}^{1/2}$ at 267 m/s. At low velocities, the propagation fracture toughness is relatively insensitive to fracture velocity, but it increases drastically as the fracture velocity v_f approaches a limiting value v_l . Thus, the fracture velocity becomes saturated at high K_I^P .

The relationship between fracture velocity and fracture propagation toughness can be described empirically as [Anderson 2005]:

$$K_I^P = \frac{K_{IA}}{1 - (v_f/v_l)^m}, \quad (6)$$

where m is a constant, and K_{IA} is the fracture arrest toughness which corresponds to K_I^P at zero fracture velocity. Fitting our data to the equation yields

$$v_l = 385 \text{ m/s}, \quad m = 5.44, \quad K_{IA} = 1.3 \text{ MPa m}^{1/2}$$

(see Figure 10). The value of K_{IA} as predicted from our results at $v_f > 250 \text{ m/s}$ is in excellent agreement with the averaged fracture toughness obtained at low fracture velocities ($v_f \sim 0$) in [Marshall and Williams 1973]. This is not surprising, though, because K_{IA} represents the fracture toughness limit at zero crack velocity. It is noted that the relation presented in the equation is not universal. It applies to the sample geometry presented in this work, and the sample geometry presented by Rosakis and his coworkers, but it may not be applicable to other sample geometries.

The observation of the limiting fracture velocity (385 m/s) is also interesting. In [Rittel and Maigre 1996] a fracture velocity of 306 m/s was reported at an initiation toughness of $6.15 \text{ MPa m}^{1/2}$, consistent with our results (365 m/s at $5.17 \text{ MPa m}^{1/2}$). Our experiment configuration is similar to that of Rittel and Maigre: the sample boundaries are free except for the loading points and thus the edge release is pronounced.

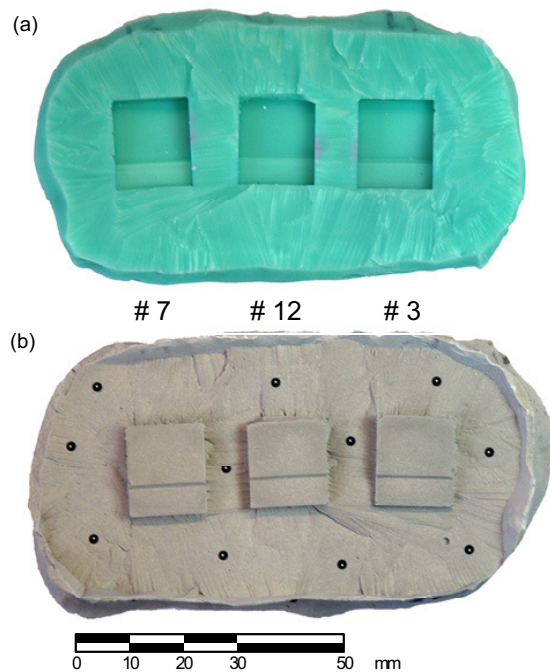


Figure 11. (a) Silicone rubber molds of three SCB fracture surfaces selected for roughness evaluation (samples #3, #7, and #12), and (b) the corresponding fracture surface replicas cast from the rubber molds.

4.3. Fracture surface roughness and fracture energy. To investigate the relationship between fracture energy and fracture roughness as a function of strain rate, the fracture surface topography of three PMMA SCB specimens loaded at different strain rates is measured with a white light 3D stereotopometric system, the advanced topometric sensor (ATOS) II (GOM mbH).

Digitization of the PMMA fracture surfaces is problematic because of the transparency of PMMA. We thus create replicas of the fractured SCB surfaces via molding and casting: the negative mold of a fracture surface is first made with silicone rubber (Figure 11a), and this mold is then used to cast fracture replicas out of a quick setting flowable anchoring cement (Figure 11b).

Digitization of each replicated fracture surface requires two individual measurements with the ATOS system. The scanning grid size is about $40\ \mu\text{m}$ by $40\ \mu\text{m}$. Transformation of these measurements into a common coordinate system is achieved by affixing several 0.4 mm (diameter) reference points around the boundaries of the fracture surfaces (see Figure 11b). The average deviation between redundant data (that is, overlapping measurements) is termed the mesh deviation, which provides an estimate of the intensity of the average measurement noise of the system [ATOS 2008]. For the three fracture surfaces digitized in this study, the mesh deviation is less than $5\ \mu\text{m}$. Following completion of all measurements, the resulting point clouds for each sample are polygonized into triangulated irregular networks using the default triangulation algorithm of the ATOS software (Delaunay triangulation with no smoothing). This process deletes redundant points of the point cloud and discretizes the surfaces into contiguous triangles with vertices defined by neighboring points of the point cloud.

For the current study, the surface roughness coefficient, R_s , is adopted to characterize the roughness of the three replicated SCB fracture surfaces. The value of R_s is given by [Soudani 1978] as follows:

$$R_s = A_t/A_n, \quad (7)$$

where A_t is the true area of the surface defined by the summation of the area of each triangular element, A_i , comprising the 3D surface [Lange et al. 1993], and A_n is the nominal area defined by the projection of the actual area onto a best-fit plane through the surface. For a perfectly flat surface, R_s equals a minimum value of 1, while most fractures in brittle materials have R_s values between 1 and 2 [Belem et al. 2000].

Considering a digitized SCB fracture surface (Figure 12), a plane parallel to the notch plane is used to define the nominal area surface rather than a best-fit plane through the fracture surface. For each sample, the maximum area of the digitized fracture surface, excluding the notch plane and any damaged areas around the perimeter of the primary fracture, is considered when calculating the true surface area and corresponding nominal surface area. As the calculated fracture energy corresponds to the propagation of the primary fracture, inclusion of the damaged areas around the perimeter of the primary fracture resulting from secondary and tertiary fracturing under high strain rates would lead to increased values of R_s that do not represent the roughness of the primary fracture. (Secondary microcracks are not found with optical microscopy, though.) Thus, a potentially misleading relationship between fracture energy and fracture roughness may result. For the three representative samples (#3, #7, and #12), W_G varies from 0.23 to 6.95 J, but the measured values of R_s vary slightly from 1.002 to 1.01.

If we assume that W_G dissipates only in the form of surface energy, W_G should scale linearly with A_t and thus G_c should scale linearly with R_s . However, considering the two extreme cases (samples #3 and #12), G_c for #12 is about 30 times that for #3, while the corresponding ratio for R_s is only 1.01. This observation calls for additional energy dissipation mechanisms during dynamic fracture. Indeed, researchers recently showed the importance of the process zone to the total energy budget in earthquake ruptures, where dynamic rupture may induce damage around the rupture tip [Poliakov et al. 2002]. In the case of PMMA dynamic fracture as studied here, the additional dissipation mechanisms may include the plasticity or viscosity, because no microcracks are observed in the recovered specimen, and remain to be investigated in the future.

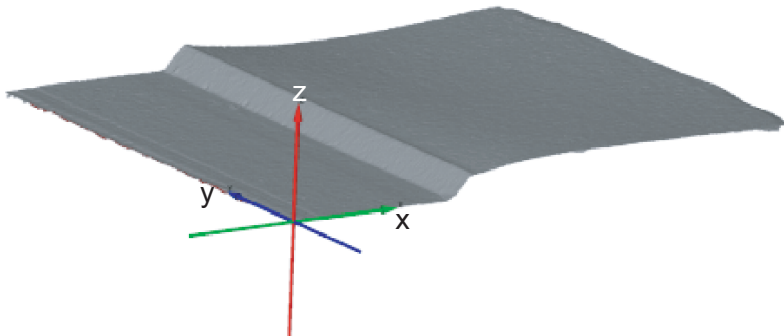


Figure 12. The surface scanning image for sample #12.

5. Conclusion

We have performed dynamic SPHB bending tests on notched semicircular PMMA specimens as well as finite element analysis and postmortem fracture surface roughness measurements, and obtained the initiation fracture toughness, propagation fracture toughness, and fracture velocity at different loading rates. The initiation and propagation toughnesses are similar and both increase with loading rate, the fracture velocity increases with the propagation toughness but reaches its limit at about 385 m/s, and their numerical relations are established. Our results also call for other energy dissipation mechanisms during dynamic fracture of PMMA besides free surface creation.

References

- [Anderson 2005] T. L. Anderson, *Fracture mechanics: fundamentals and applications*, 3rd ed., CRC Press, Boca Raton, FL, 2005.
- [ASTM 1997] “Standard test method for plane-strain fracture toughness of metallic materials”, Standard ASTM E399-90, American Society for Testing and Materials, Philadelphia, 1997, Available at <http://tinyurl.com/ASTM-E399-90>. Superseded by the [active standard](#).
- [ATOS 2008] *ATOS user manual*, Version 6.1, GOM, Braunschweig, 2008.
- [Barsoum 1977] R. S. Barsoum, “Triangular quarter-point elements as elastic and perfectly-plastic crack tip elements”, *Int. J. Numer. Methods Eng.* **11**:1 (1977), 85–98.
- [Belem et al. 2000] T. Belem, F. Homand-Etienne, and M. Souley, “Quantitative parameters for rock joint surface roughness”, *Rock Mech. Rock Eng.* **33**:4 (2000), 217–242.
- [Böhme and Kalthoff 1982] W. Böhme and J. F. Kalthoff, “The behavior of notched bend specimens in impact testing”, *Int. J. Fract.* **20**:4 (1982), R139–R143.
- [Chen et al. 2009] R. Chen, K. Xia, F. Dai, F. Lu, and S. N. Luo, “Determination of dynamic fracture parameters using a semi-circular bend technique in split Hopkinson pressure bar testing”, *Eng. Fract. Mech.* **76**:9 (2009), 1268–1276.
- [Chong and Kuruppu 1984] K. P. Chong and M. D. Kuruppu, “New specimen for fracture toughness determination for rock and other materials”, *Int. J. Fract.* **26**:2 (1984), R59–R62.
- [Dally 1979] J. W. Dally, “Dynamic photoelastic studies of fracture”, *Exp. Mech.* **19**:10 (1979), 349–361.
- [Évora et al. 2005] V. M. F. Évora, N. Jain, and A. Shukla, “Stress intensity factor and crack velocity relationship for polyester/TiO₂ nanocomposites”, *Exp. Mech.* **45**:2 (2005), 153–159.
- [Frew et al. 2005] D. J. Frew, M. J. Forrestal, and W. Chen, “Pulse shaping techniques for testing elastic-plastic materials with a split Hopkinson pressure bar”, *Exp. Mech.* **45**:2 (2005), 186–195.
- [Kobayashi and Dally 1977a] T. Kobayashi and J. W. Dally, “Relation between crack velocity and the stress intensity factor in birefringent polymers”, pp. 257–273 in *Fast fracture and crack arrest* (Chicago, 1976), edited by G. T. Hahn and M. F. Kanninen, ASTM STP **627**, American Society for Testing and Materials, Philadelphia, 1977. Paper ID STP27392S.
- [Kobayashi and Dally 1977b] T. Kobayashi and J. W. Dally, “System of modified epoxies for dynamic photoelastic studies of fracture”, *Exp. Mech.* **17**:10 (1977), 367–374.
- [Kobayashi et al. 1972] A. S. Kobayashi, B. G. Wade, and D. E. Maiden, “Photoelastic investigation on the crack-arrest capability of a hole”, *Exp. Mech.* **12**:1 (1972), 32–37.
- [Kolsky 1953] H. Kolsky, *Stress waves in solids*, Clarendon, Oxford, 1953.
- [Lange et al. 1993] D. A. Lange, H. M. Jennings, and S. P. Shah, “Relationship between fracture surface roughness and fracture behavior of cement paste and mortar”, *J. Am. Ceram. Soc.* **76**:3 (1993), 589–597.
- [Maigre and Rittel 1995] H. Maigre and D. Rittel, “Dynamic fracture detection using the force-displacement reciprocity: application to the compact compression specimen”, *Int. J. Fract.* **73**:1 (1995), 67–79.
- [Marshall and Williams 1973] G. P. Marshall and J. G. Williams, “The correlation of fracture data for PMMA”, *J. Mater. Sci.* **8**:1 (1973), 138–140.

- [Needleman and Rosakis 1999] A. Needleman and A. J. Rosakis, “The effect of bond strength and loading rate on the conditions governing the attainment of intersonic crack growth along interfaces”, *J. Mech. Phys. Solids* **47**:12 (1999), 2411–2449.
- [Owen et al. 1998] D. M. Owen, S. Zhuang, A. J. Rosakis, and G. Ravichandran, “Experimental determination of dynamic crack initiation and propagation fracture toughness in thin aluminum sheets”, *Int. J. Fract.* **90**:1–2 (1998), 153–174.
- [Poliakov et al. 2002] A. N. B. Poliakov, R. Dmowska, and J. R. Rice, “Dynamic shear rupture interactions with fault bends and off-axis secondary faulting”, *J. Geophys. Res. Solid Earth* **107**:B11 (2002), 2295.
- [Rittel and Maigre 1996] D. Rittel and H. Maigre, “An investigation of dynamic crack initiation in PMMA”, *Mech. Mater.* **23**:3 (1996), 229–239.
- [Rosakis et al. 1984] A. J. Rosakis, J. Duffy, and L. B. Freund, “The determination of dynamic fracture toughness of AISI 4340 steel by the shadow spot method”, *J. Mech. Phys. Solids* **32**:6 (1984), 443–460.
- [Soudani 1978] S. M. El-Soudani, “Profilometric analysis of fractures”, *Metallography* **11**:3 (1978), 247–336.
- [Wada 1992] H. Wada, “Determination of dynamic fracture toughness for PMMA”, *Eng. Fract. Mech.* **41**:6 (1992), 821–831.
- [Wada et al. 1993] H. Wada, M. Seika, C. A. Calder, and T. C. Kennedy, “Measurement of impact fracture toughness for PMMA with single-point bending test using an air gun”, *Eng. Fract. Mech.* **46**:4 (1993), 715–719.
- [Weerasooriya et al. 2006] T. Weerasooriya, P. Moy, D. Casem, M. Cheng, and W. Chen, “A four-point bend technique to determine dynamic fracture toughness of ceramics”, *J. Am. Ceram. Soc.* **89**:3 (2006), 990–995.
- [Xia et al. 2006] K. Xia, V. B. Chalivendra, and A. J. Rosakis, “Observing ideal ‘self-similar’ crack growth in experiments”, *Eng. Fract. Mech.* **73**:18 (2006), 2748–2755.
- [Zehnder and Rosakis 1990] A. T. Zehnder and A. J. Rosakis, “Dynamic fracture initiation and propagation in 4340 steel under impact loading”, *Int. J. Fract.* **43**:4 (1990), 271–285.
- [Zhang et al. 2000] Z. X. Zhang, S. Q. Kou, L. G. Jiang, and P.-A. Lindqvist, “Effects of loading rate on rock fracture: fracture characteristics and energy partitioning”, *Int. J. Rock Mech. Min.* **37**:5 (2000), 745–762.

Received 11 May 2010. Revised 19 Sep 2010. Accepted 30 Sep 2010.

SHENG HUANG: sh.huang@utoronto.ca

Department of Civil Engineering and Lassonde Institute, University of Toronto, Toronto M5S 1A4, Canada

SHENG-NIAN LUO: sluo@lanl.gov

Physics Division, Los Alamos National Laboratory, Los Alamos, NM 87545, United States

BRYAN S. A. TATONE: bryan.tatone@utoronto.ca

Department of Civil Engineering and Lassonde Institute, University of Toronto, Toronto M5S 1A4, Canada

KAIWEN XIA: kaiwen@ecf.utoronto.ca

Department of Civil Engineering and Lassonde Institute, University of Toronto, Toronto M5S 1A4, Canada

JOURNAL OF MECHANICS OF MATERIALS AND STRUCTURES

jomms.org

Founded by Charles R. Steele and Marie-Louise Steele

EDITORS

CHARLES R. STEELE Stanford University, USA
DAVIDE BIGONI University of Trento, Italy
IWONA JASIUK University of Illinois at Urbana-Champaign, USA
YASUHIRO SHINDO Tohoku University, Japan

EDITORIAL BOARD

H. D. BUI École Polytechnique, France
J. P. CARTER University of Sydney, Australia
R. M. CHRISTENSEN Stanford University, USA
G. M. L. GLADWELL University of Waterloo, Canada
D. H. HODGES Georgia Institute of Technology, USA
J. HUTCHINSON Harvard University, USA
C. HWU National Cheng Kung University, Taiwan
B. L. KARIHALOO University of Wales, UK
Y. Y. KIM Seoul National University, Republic of Korea
Z. MROZ Academy of Science, Poland
D. PAMPLONA Universidade Católica do Rio de Janeiro, Brazil
M. B. RUBIN Technion, Haifa, Israel
A. N. SHUPIKOV Ukrainian Academy of Sciences, Ukraine
T. TARNAI University Budapest, Hungary
F. Y. M. WAN University of California, Irvine, USA
P. WRIGGERS Universität Hannover, Germany
W. YANG Tsinghua University, China
F. ZIEGLER Technische Universität Wien, Austria

PRODUCTION contact@msp.org

SILVIO LEVY Scientific Editor

Cover design: Alex Scorpan

Cover photo: Ev Shafir

See <http://jomms.org> for submission guidelines.

JoMMS (ISSN 1559-3959) is published in 10 issues a year. The subscription price for 2011 is US \$520/year for the electronic version, and \$690/year (+ \$60 shipping outside the US) for print and electronic. Subscriptions, requests for back issues, and changes of address should be sent to Mathematical Sciences Publishers, Department of Mathematics, University of California, Berkeley, CA 94720–3840.

JoMMS peer-review and production is managed by EditFLOW™ from Mathematical Sciences Publishers.

PUBLISHED BY
 **mathematical sciences publishers**
<http://msp.org/>

A NON-PROFIT CORPORATION

Typeset in L^AT_EX

Copyright ©2011 by Mathematical Sciences Publishers

Modelling of acoustodiffusive surface waves in piezoelectric-semiconductor composite structures	J. N. SHARMA, K. K. SHARMA and A. KUMAR	791
Dynamic fracture tests of polymethylmethacrylate using a semicircular bend technique	S. HUANG, S.-N. LUO, B. S. A. TATONE and K. XIA	813
Stress and buckling analyses of laminates with a cutout using a {3, 0}-plate theory	ATILA BARUT, ERDOGAN MADENCI and MICHAEL P. NEMETH	827
Electrothermomechanical behavior of a radially polarized rotating functionally graded piezoelectric cylinder	A.G. ARANI, A. LOGHMAN, A. ABDOLLAHITAHERI and V. ATABAKHSHIAN	869
Large-amplitude dynamic analysis of stiffened plates with free edges	ANIRBAN MITRA, PRASANTA SAHOO and KASHINATH SAHA	883
Dynamic behavior of magnetostrictive/piezoelectric laminate cylindrical shells due to electromagnetic force	B. BIJU, N. GANESAN and K. SHANKAR	915
Geometrically nonlinear thermomechanical response of circular sandwich plates with a compliant core	YEOSHUA FROSTIG and OLE THOMSEN	925